(Received 23 February 2023, Accepted 12 April 2024, Scheduled 21 April 2024)

# Theoretical Analysis on Generating Composite-Orbital Angular Momentum Beam

Zhixia Wang, Zelin Zhu, Shilie Zheng*, Xiaonan Hui, and Xianmin Zhang

*Department of Information Science and Electronic Engineering, Zhejiang University, Hangzhou 310027, China*

**ABSTRACT:** For orbital angular momentum (OAM) based practical applications in radio frequency, inherent puzzles of traditional OAM carrying waves will be encountered inevitably, such as the inherent dark zone in the beam center and severe beam divergence. To solve the problem, some specific beams, which are directional beams with high gain, retaining the vorticity and orthogonality of conventional OAM carrying beams have been put forward. They are termed as composite-orbital angular momentum (c-OAM) beam for the first time in this paper. Continuous arc source model (CASM) and discrete arc source model (DASM) are proposed to generate c-OAM beams, which are composed of several OAM waves with different weights. Mathematical models of CASM and DASM are demonstrated, and the field expressions are derived. Numerical simulations are conducted to analyze the characteristics of the c-OAM beams, including directivity, vorticity, orthogonality, etc., and certify the validity of the proposed model. In all, CASM and DASM are capable of generating c-OAM beams, which are more suitable for OAM property based practical applications. Since beamforming is one of the key technologies in 5G systems, c-OAM beams are beneficial to be applied in current communication systems.

## 1. INTRODUCTION

Due to the explosive demand for communication rates, many technologies, such as multiplex technology, coding technology, modulation technology, and multi-antenna technology have been constantly invented and studied from various aspects to improve the communication capacity and mitigate the scarcity of spectrum resources during the last decades [1, 2]. Orbital angular momentum, (OAM) discovered in 1992, is an intrinsic characteristic of electromagnetic waves [3]. As a new degree of freedom, OAM has attracted much attention due to its potential to increase communication capacity.

OAM carrying waves have azimuthal phase distribution of $e^{-jl\varphi}$, where $l$ is an integer representing OAM mode number, and $\varphi$ is the azimuth angle. The attractive characteristics of OAM are its vorticity and orthogonality. In optical domain, applications based on OAM range from imaging [4] to communications [5]. In radio frequency, OAM-based communication technologies are constantly being researched and promoted [6, 7]. However, researches on OAM in radio frequency face huge challenges ascribing to the severe divergence and inherent dark zone in the center owing to on-axis phase singularity. Due to the donut-shaped energy distribution and divergence of OAM beams [8], it is difficult or even impossible to receive the whole angular aperture in the long distance transmission to ensure the orthogonality [9]. Even worse, the divergence angle varies with OAM mode, making it troublesome to multiplex. Some schemes have been proposed to resolve these problems. In [10], a partial aperture sampling receiving scheme is demonstrated to tackle the barrier of receiving in multiplexed communication systems. However, the energy efficiency is very low. In [11], plane spiral OAM (PS-OAM) waves are proposed to solve the problem that divergence angle varies with OAM mode, and it is a special case of OAM. Furthermore, angular position $\varphi$ and OAM mode $l$ are linked by a Fourier transformation owing to the phase distribution of $e^{-jl\varphi}$ [12, 13], OAM can be utilized as electromagnetic (EM) field eigen-mode to realize beam steering and construct arbitrary structured radio beams in azimuthal domain [14]. Beam steering based on PS-OAM waves can be easily realized, and the pencil beams with liner phases in the main lobes are generated [15]. However, the method of superposing PS-OAM waves requires a large number of PS-OAM antennas or complex antenna structure. It is an indirect method and restricts the miniaturization and integration in practical applications [16, 17].

Fortunately, Fouda et al. used a quasi-circular array antenna to generate a special OAM carrying wave, called quasi-OAM [18]. A partial slotted curved waveguide leaky-wave antenna is proposed to generate an OAM mode group (OAM-MG), whose beam is directional and with the linear phase distribution. Similar to the conventional OAM beams [19], the slope of the linear phase distribution is called equivalent OAM mode. Considering quasi-OAM beams in [18] and high equivalent OAM mode MG beams in [19], both have several OAM modes in the OAM spectra analysis. Thus, they can be viewed as direct methods to generate several OAM modes to realize the desired beams. The common properties of the pencil beams in [14], the quasi-OAM waves in [18], and the high equivalent OAM mode MG beams in [19] can be summarized: Firstly, they are directional beams, i.e., the most energy is concentrated

* Corresponding author: Shilie Zheng (zhengsl@zju.edu.cn).

in the main lobes. Secondly, the phase distributions are linear in the beams's main lobes. Thirdly, in the OAM spectra analysis, there are several OAM modes rather than a single one. More importantly, these beams retain the vorticity of OAM and have quasi-orthogonality. For unification, these kinds of beams are referred as composite-OAM beams collectively and abbreviated as c-OAM. The c-OAM beam is defined as a beam that is composed of multiple OAM beams with different modes and weights and thus have vorticity, orthogonality, directivity, and other characteristics. The theory of the indirect method to generate c-OAM waves is expounded in [14]. Although direct methods to generate c-OAM waves were reported in [18, 19], there was no comprehensive theoretical analysis till now.

The main purpose of this paper is to form a systematic theory of the direct method to generate c-OAM waves, to deduce the analytical solutions of the field distributions, and to clarify the properties of c-OAM waves in detail. The rest of the paper is organized as follows. First of all, mathematical models are abstracted and given, and the field distribution expressions are derived by conducting Fourier series expansion on electric current distributions of the source. Then, numerical simulations are carried out by utilizing electric dipole array as the equivalent source. Far-field radiation patterns, amplitude and phase distributions are demonstrated. OAM spectra are analyzed to verify the rationality of the theoretical analysis. Beam direction and polarization are also discussed. Last but not least, c-OAM beams generated by indirect methods and direct methods are compared, and the c-OAM beams' potential applications in communications are proposed.

## 2. MODEL AND FORMULATION

A circular traveling-wave antenna is an effective configuration for generating high-quality OAM beams. It is a mathematical model, and electrical field formulations are shown and derived in [20]. Similarly, a complete and detailed analysis on c-OAM is conducted in this paper.

As shown in Fig. 1(a), the theoretical mathematical model for partial arc traveling-wave antenna in [19] is a wire bent into an arc of radius $a$ and central angle $\beta$ in horizontal plane, fed with a constant electric current amplitude $I_0$ but a consecutive phase along the arc of $l_o\varphi$, i.e., $I = I_0 e^{-jl_o\varphi}$, where $\varphi$ $(0 < \varphi < \beta)$ is the azimuth angle in the cylindrical coordinate, and $l_o$ is an integer representing the desired OAM mode. Since its current distribution over the arc is continuous, we called it 'continuous arc source model', abbreviated as 'CASM'. From another perspective, CASM can be obtained by cutting a section of the circular traveling-wave antenna model. Thus, the electric current distribution of CASM can be described as follows

$$I = I_0 e^{-jl_o\varphi} \cdot g(\varphi), \quad g(\varphi) = \begin{cases} 1, & 0 < \varphi < \beta \\ 0, & else \end{cases} \tag{1}$$

Due to the Fourier relationship between OAM mode and azimuth angle, the source's electric current distribution expression can be written in the form of Fourier series [23]. By carrying out Fourier series on (1), the electric current distribution of CASM can be expressed as

$$I = I_0 \frac{\beta}{2\pi} \sum_{l=-\infty}^{+\infty} \operatorname{sinc}\left[\frac{\beta}{2}(l_o - l)\right] \cdot e^{-j(l_o-l)\frac{\beta}{2}} \cdot e^{-jl\varphi} \tag{2}$$

In other words, the source demonstrated in (1) can be decomposed into the superposition of many different OAM modes in (2). Accordingly, the electric field distribution of CASM can be derived in (3),

$$\begin{aligned} E_\rho =& -B_0 \cos^2\theta \frac{e^{-jkr}}{r} \cdot \sum_{l=-\infty}^{+\infty} \operatorname{sinc}\left[\frac{\beta}{2}(l_o - l)\right] \cdot e^{-j(l_o-l)\frac{\beta}{2}} \\ & \cdot j^l e^{-jl\varphi} \frac{J_{l-1}(ka\sin\theta) + J_{l+1}(ka\sin\theta)}{2} \\ E_\varphi =& -B_0 \frac{e^{-jkr}}{r} \cdot \sum_{l=-\infty}^{+\infty} \operatorname{sinc}\left[\frac{\beta}{2}(l_o - l)\right] \cdot e^{-j(l_o-l)\frac{\beta}{2}} \\ & \cdot j^l e^{-jl\varphi} \frac{J_{l-1}(ka\sin\theta) - J_{l+1}(ka\sin\theta)}{2j} \\ E_z =& B_0 \sin\theta\cos\theta \frac{e^{-jkr}}{r} \cdot \sum_{l=-\infty}^{+\infty} \operatorname{sinc}\left[\frac{\beta}{2}(l - l_o)\right] \\ & \cdot e^{-j(l_o-l)\frac{\beta}{2}} \cdot j^l e^{-jl\varphi} \frac{J_{l-1}(ka\sin\theta) + J_{l+1}(ka\sin\theta)}{2} \end{aligned} \tag{3}$$

where $B_0 = j\omega\mu I_0 a\beta/4\pi$ and higher order terms are omitted. From the electric field distribution in (3), we can find that CASM will generate some adjacent side modes except main mode $l_o$, and these modes are multiplied by the weighting factor $\operatorname{sinc}[\beta(l_o - l)/2] \cdot [J_{l-1}(ka\sin\theta) + J_{l+1}(ka\sin\theta)]/2$.

As uniform circular array antenna (UCA) is the most commonly used method to generate OAM beams, c-OAM beams can be generated by the array too. In [18], Fouda et al. used the quasi-circular array antenna to generate the quasi-OAM. The theoretical mathematical model for the array in [18] to generate c-OAM beams is shown in Fig. 1(b). The array elements are all placed in $z$-orientation. There are $M$ elements equidistantly arranged around the arc with radius $a$ and central angle $\beta$, and the angle between each two adjacent elements is $\beta/(M-1)$, where $\beta/(M-1) = 2\pi/N$. The $M$ elements fed with constant electric current amplitude $I_0$ but variable phases, and the $m$th element's phase is $\varphi_m = 2\pi l_o \cdot (m-1)/N$, $N \geq M$, where $m = 1, 2, \ldots, M$. $M$ is the number of the elements on the arc, while $N$ is the number of the elements on the whole circle if the array elements are arranged on the circle, and the angle between each two adjacent elements is the same as that on arc. That's to say, when $M = N$, it is the case of UCA, and the condition that the number of array elements needs to meet is $N \geq l_o/2$, $M > 2$. The current distribution of the model in Fig. 1(b) can be expressed by (4). Since the current distribution over the arc is discrete, we call it 'discrete arc source model', abbreviated as 'DASM'. Equation (5) is Fourier series expansion of the current distribution (4). Thus, the electric field distribution of DASM can be derived in (6), where

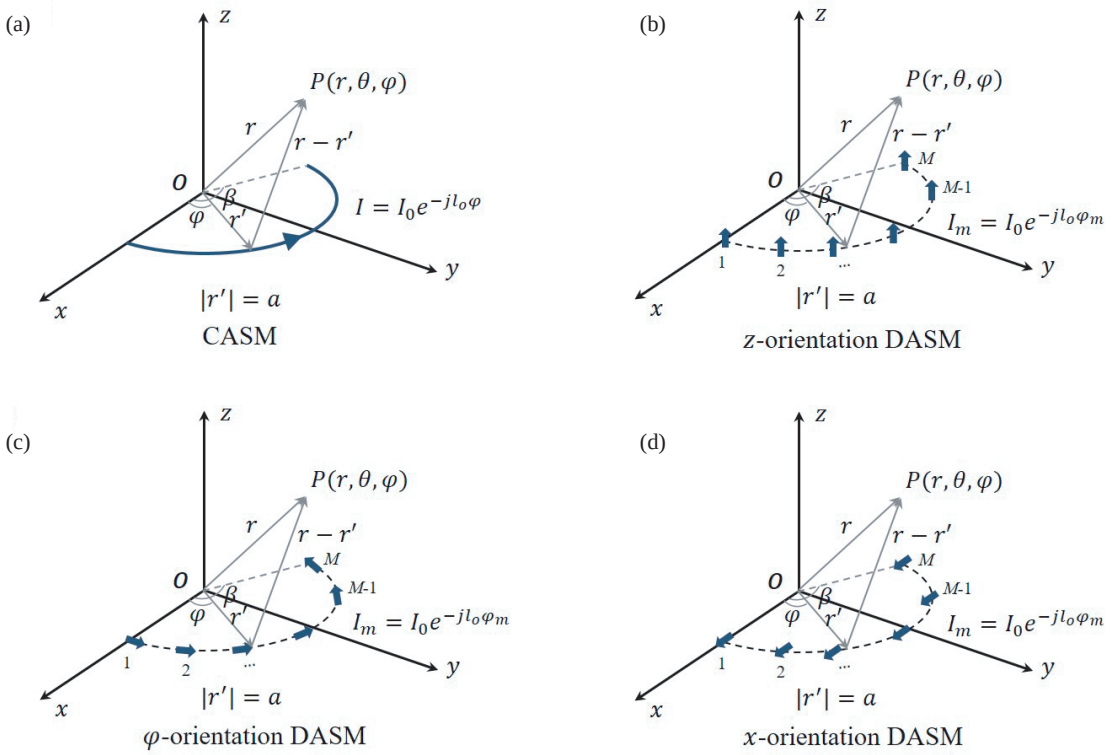


**FIGURE 1**. Theoretical model of (a) CASM; (b) $z$-orientation DASM; (c) $\varphi$-orientation DASM; (d) $x$-orientation DASM.

$C_0 = j\omega\mu I_0 a/2N$ and higher order terms are omitted. The generated OAM modes extend periodically with a period of $N$ and then multiplied by the corresponding weighting factor.

$$I = I_0 e^{-jl_o\varphi} \cdot g(\varphi) \cdot \sum_{n=0}^{N-1} \delta\left(\varphi - \frac{2\pi}{N}n\right),$$

$$g(\varphi) = \begin{cases} 1, & \varphi_0 < \varphi < \varphi_0 + \beta \\ 0, & else \end{cases} \tag{4}$$

$$I = I_0 \sum_{l=-\infty}^{+\infty} \begin{cases} \dfrac{\sin\left(\dfrac{M}{N}(l-l_o)\pi\right)}{N\sin\left(\dfrac{1}{N}(l-l_o)\pi\right)} \cdot e^{-jl\varphi}, \\ l \neq l_o,\ l \neq l_o \pm N,\ l \neq l_o \pm 2N, \ldots \\ \dfrac{M}{N} \cdot e^{-jl\varphi}, \\ l = l_o,\ l = l_o \pm N,\ l = l_o \pm 2N, \ldots \end{cases} \tag{5}$$

$$E_x^z = C_0 \sin\theta\cos\theta\cos\varphi \frac{e^{-jkr}}{r}$$

$$\cdot \sum_{l=-\infty}^{+\infty} \begin{cases} \dfrac{\sin\left(\dfrac{M}{N}(l-l_o)\pi\right)}{\sin\left(\dfrac{1}{N}(l-l_o)\pi\right)} \cdot j^l e^{-jl\varphi} J_l(ka\sin\theta), \\ l \neq l_o,\ l \neq l_o \pm N, \ldots \\ M \cdot j^l e^{-jl\varphi} J_l(ka\sin\theta), \\ l = l_o,\ l = l_o \pm N, \ldots \end{cases}$$

$$E_y^z = C_0 \sin\theta\cos\theta\sin\varphi \frac{e^{-jkr}}{r}$$

$$\cdot \sum_{l=-\infty}^{+\infty} \begin{cases} \dfrac{\sin\left(\dfrac{M}{N}(l-l_o)\pi\right)}{\sin\left(\dfrac{1}{N}(l-l_o)\pi\right)} \cdot j^l e^{-jl\varphi} J_l(ka\sin\theta), \\ l \neq l_o,\ l \neq l_o \pm N, \ldots \\ M \cdot j^l e^{-jl\varphi} J_l(ka\sin\theta), \\ l = l_o,\ l = l_o \pm N, \ldots \end{cases}$$

$$E_z^z = C_0 \sin^2\theta \frac{e^{-jkr}}{r}$$

$$\cdot \sum_{l=-\infty}^{+\infty} \begin{cases} \dfrac{\sin\left(\dfrac{M}{N}(l-l_o)\pi\right)}{\sin\left(\dfrac{1}{N}(l-l_o)\pi\right)} \cdot j^l e^{-jl\varphi} J_l(ka\sin\theta), \\ l \neq l_o,\ l \neq l_o \pm N, \ldots \\ M \cdot j^l e^{-jl\varphi} J_l(ka\sin\theta), \\ l = l_o,\ l = l_o \pm N, \ldots \end{cases} \tag{6}$$

For DASMs, the array element can be placed at $x$, $y$, $\varphi$, and $r$ orientations except $z$-orientation. Due to electromagnetic duality, $y$-orientation is equivalent to $x$-orientation, and $r$-orientation is equivalent to $\varphi$-orientation. For convenience, $z$-orientation, $x$-orientation, and $\varphi$-orientation DASM are discussed to represent all cases of array element placement orientations in this paper. The $\varphi$-orientation DASM and $x$-orientation

DASM are shown in Figs. 1(c) and (d). For different array element placement orientations, the expressions of electric field distributions are different. The electric field distributions of $\varphi$-orientation DASM and $x$-orientation DASM are derived in (7) and (8), respectively, and higher order terms are omitted. For convenience, the electric field formulations of the $\varphi$-orientation array are obtained in the cylindrical coordinate, while $x$-orientation and $z$-orientation arrays are obtained in the cartesian coordinate. It is worth noting that, on the left side of (6), (7), (8), the superscript of the electric field represents the placement orientation of the array, and the subscript represents the component of the electric field. Evidently, all components of the electric field are superposed by many different OAM modes multiplied by the corresponding weighting factor. That's why the c-OAM beams can be generated.

$$E_{\rho}^{\varphi} = -C_0 \cos^2\theta \frac{e^{-jkr}}{r} \cdot \sum_{l=-\infty}^{+\infty} \begin{cases} \dfrac{\sin\left(\dfrac{M}{N}(l-l_o)\pi\right)}{\sin\left(\dfrac{1}{N}(l-l_o)\pi\right)} \cdot j^l e^{-jl\varphi} \dfrac{J_{l-1}(ka\sin\theta)+J_{l+1}(ka\sin\theta)}{2}, \\ \qquad l \neq l_o,\ l \neq l_o \pm N, \ldots \\ M \cdot j^l e^{-jl\varphi} \dfrac{J_{l-1}(ka\sin\theta)+J_{l+1}(ka\sin\theta)}{2}, \\ \qquad l = l_o,\ l = l_o \pm N, \ldots \end{cases}$$

$$E_{\varphi}^{\varphi} = -C_0 \frac{e^{-jkr}}{r} \cdot \sum_{l=-\infty}^{+\infty} \begin{cases} \dfrac{\sin\left(\dfrac{M}{N}(l-l_o)\pi\right)}{\sin\left(\dfrac{1}{N}(l-l_o)\pi\right)} \cdot j^l e^{-jl\varphi} \dfrac{J_{l-1}(ka\sin\theta)-J_{l+1}(ka\sin\theta)}{2j}, \\ \qquad l \neq l_o,\ l \neq l_o \pm N, \ldots \\ M \cdot j^l e^{-jl\varphi} \dfrac{J_{l-1}(ka\sin\theta)-J_{l+1}(ka\sin\theta)}{2j}, \\ \qquad l = l_o,\ l = l_o \pm N, \ldots \end{cases}$$

$$E_{z}^{\varphi} = C_0 \sin\theta \cos\theta \frac{e^{-jkr}}{r} \cdot \sum_{l=-\infty}^{+\infty} \begin{cases} \dfrac{\sin\left(\dfrac{M}{N}(l-l_o)\pi\right)}{\sin\left(\dfrac{1}{N}(l-l_o)\pi\right)} \cdot j^l e^{-jl\varphi} \dfrac{J_{l-1}(ka\sin\theta)+J_{l+1}(ka\sin\theta)}{2}, \\ \qquad l \neq l_o,\ l \neq l_o \pm N, \ldots \\ M \cdot j^l e^{-jl\varphi} \dfrac{J_{l-1}(ka\sin\theta)+J_{l+1}(ka\sin\theta)}{2}, \\ \qquad l = l_o,\ l = l_o \pm N, \ldots \end{cases} \quad (7)$$

$$E_{x}^{x} = -C_0(\sin^2\varphi\sin^2\theta + \cos^2\theta) \frac{e^{-jkr}}{r} \cdot \sum_{l=-\infty}^{+\infty} \begin{cases} \dfrac{\sin\left(\dfrac{M}{N}(l-l_o)\pi\right)}{\sin\left(\dfrac{1}{N}(l-l_o)\pi\right)} \cdot j^l e^{-jl\varphi} J_l(ka\sin\theta), \\ \qquad l \neq l_o,\ l \neq l_o \pm N, \ldots \\ M \cdot j^l e^{-jl\varphi} J_l(ka\sin\theta), \\ \qquad l = l_o,\ l = l_o \pm N, \ldots \end{cases}$$

$$E_{y}^{x} = C_0 \sin\varphi\cos\varphi\sin^2\theta \frac{e^{-jkr}}{r} \cdot \sum_{l=-\infty}^{+\infty} \begin{cases} \dfrac{\sin\left(\dfrac{M}{N}(l-l_o)\pi\right)}{\sin\left(\dfrac{1}{N}(l-l_o)\pi\right)} \cdot j^l e^{-jl\varphi} J_l(ka\sin\theta), \\ \qquad l \neq l_o,\ l \neq l_o \pm N, \ldots \\ M \cdot j^l e^{-jl\varphi} J_l(ka\sin\theta), \\ \qquad l = l_o,\ l = l_o \pm N, \ldots \end{cases}$$

$$E_{z}^{x} = C_0 \cos\varphi\sin\theta\cos\theta \frac{e^{-jkr}}{r} \cdot \sum_{l=-\infty}^{+\infty} \begin{cases} \dfrac{\sin\left(\dfrac{M}{N}(l-l_o)\pi\right)}{\sin\left(\dfrac{1}{N}(l-l_o)\pi\right)} \cdot j^l e^{-jl\varphi} J_l(ka\sin\theta), \\ \qquad l \neq l_o,\ l \neq l_o \pm N, \ldots \\ M \cdot j^l e^{-jl\varphi} J_l(ka\sin\theta), \\ \qquad l = l_o,\ l = l_o \pm N, \ \ldots \end{cases} \quad (8)$$

In this section, CASM and DASM are proposed to analyze the direct methods of generating c-OAM beams in detail. Through conducting Fourier series expansion on electric current distributions, the expressions of electric field distributions can be easily derived. In the following section, the radiation field will be numerically calculated based on the vector potential to verify the correctness of the derived electric field expressions, and to further analyze the characteristics of the generated c-OAM beams.

## 3. NUMERICAL CALCULATION AND ANALYSIS

### 3.1. Field Expression

For CASM, the vector potential can be described as (9), where $\beta$ is the central angle; the superscript $'$ denotes the source coordinate; point $P$ is an observation point denoting by $(r, \theta, \varphi)$ in the spherical coordinate and $(\rho, \varphi, z)$ in cylindrical coordinate, as shown in Fig. 1(a). When the central angle $\beta = 360°$, it is the mathematical model of a circular traveling-wave antenna in [20].

$$\mathbf{A}(\mathbf{r}) = \frac{\mu I_0}{4\pi} \int_0^{\beta} \frac{e^{-jl\varphi} e^{-jk|\mathbf{r}-\mathbf{r}'|}}{|\mathbf{r}-\mathbf{r}'|} dl'$$

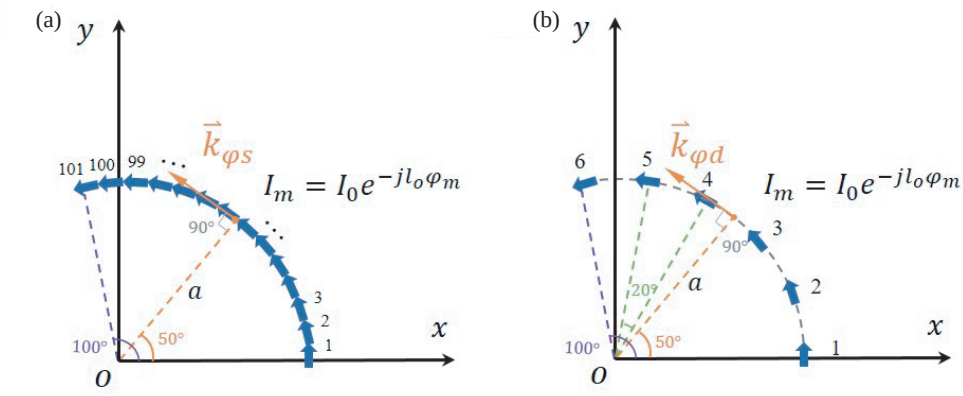


**FIGURE 2**. Array element placement of (a) CASM ($a = 0.06$ m, $N = 360$, $M = 101$) and (b) DASM ($a = 0.06$ m, $N = 18$, $M = 6$) in simulation.

$$= \frac{\mu I_0}{4\pi}\int_0^{\beta}\frac{e^{-jl\varphi}e^{-jk|r-r'|}}{|\mathbf{r}-\mathbf{r}'|}a(-\hat{x}\sin\varphi' + \hat{y}\cos\varphi')d\varphi' \quad (9)$$

For DASM, the total vector potential can be obtained by superposing vector potential of each array element, as described in (10). $M$ is the number of the elements in DASM, and $\varphi_p$ represents the azimuthal position of the array element, i.e., $\varphi_p = 2\pi\cdot(p-1)/N$, $p = 1, 2, \ldots, M$.

$$\mathbf{A} = \sum_{p=1}^{M}\mathbf{A}_p = \sum_{p=1}^{M}\frac{\mu I_0 \Delta l e^{-jkr_p}e^{-jl\varphi_p}}{4\pi r_p}(\hat{x}\sin\varphi_p + \hat{y}\sin\varphi_p) \quad (10)$$

According to the conventional electromagnetic analysis, the electric and magnetic fields can be obtained based on the vector potential

$$\mathbf{H} = \frac{1}{\mu}\nabla\times\mathbf{A}$$
$$\mathbf{E} = \frac{1}{j\omega\varepsilon}\nabla\times\mathbf{H} \quad (11)$$

As we all know, when $M\to\infty$, the DASM is equivalent to CASM. Thus, in this section, we use $\varphi$-orientation short dipoles as array elements to calculate the electric fields of DASM. When the number of $\varphi$-orientation short dipoles is enough, the array turns into a continuous wire, and the electric fields can be regarded as the results of CASM.

### 3.2. Numerical Calculation

The simulation parameters are shown in Table 1; the desired OAM mode $l_o = 8$, the radius $a = 0.06$ m. Fig. 2 displays the placement of $\varphi$-orientation short dipoles in the simulation. For CASM in Fig. 2(a), the element number $N = 360$, $M = 101$, i.e., $\beta = 100°$, and for DASM in Fig. 2(b), the element number $N = 18$, $M = 6$, i.e., the angle between two adjacent array elements is 20°, $\beta = 100°$.

**TABLE 1**. Numerical calculation parameters.

| Parameters | Value | Unit |
|---|---|---|
| absolute permeability $u_0$ | $4\pi\times10^{-7}$ | H/m |
| absolute dielectric constant $\varepsilon_0$ | $8.854\times10^{-12}$ | F/m |
| speed of light $c$ | $3\times10^{8}$ | m/s |
| frequency $f$ | 10 | GHz |
| current density $I_0$ | 1 | A |
| dipole size $\Delta l$ | $1\times10^{-3}$ | m |
| radius $a$ | 0.06 | m |
| OAM mode $l_o$ | 8 | / |

### 3.3. Results Analysis

CASM and DASM are simulated and analyzed, respectively. The simulation is conducted at 10 GHz, and the observation distance is $50\lambda$.

Figure 3 shows the far-field radiation patterns. Fig. 3(a) is the case of CASM, and Fig. 3(b) is the case of DASM. As we can see, both beams are directional beams with gain, but the beam generated by DASM has an obvious side lobe. Thus, the gain of the beam generated by CASM is higher than that of the DASM.

Figure 4 shows the 2-D intensity and phase distributions of the electric field components on the cross sections. The cross-section is a plane where elevation angle $\theta$ is a constant, and amplitude reaches maximum. Figs. 4(a) and (c) display the intensity and phase distributions of CASM, and Figs. 4(b) and (d) display the intensity and phase distributions of DASM. It can also be seen that the beam generated by DASM has a side lobe. As we know, when the radiation pattern is examined on a plane, the smaller the beam side lobes are, the higher the gain can be. We divide the electric field of c-OAM beams by the number of array elements. The maximum of electric field of CASM is 1.7863, and that of DASM is 1.6757, which are displayed clearly in Fig. 5. More importantly, the phase distributions of the electric field components seem to have vorticity in Figs. 4(c) and (d). The target will carry extra spatial phase information without relying on relative movement under the illumination of c-OAM beams due to the vorticity [21, 22].

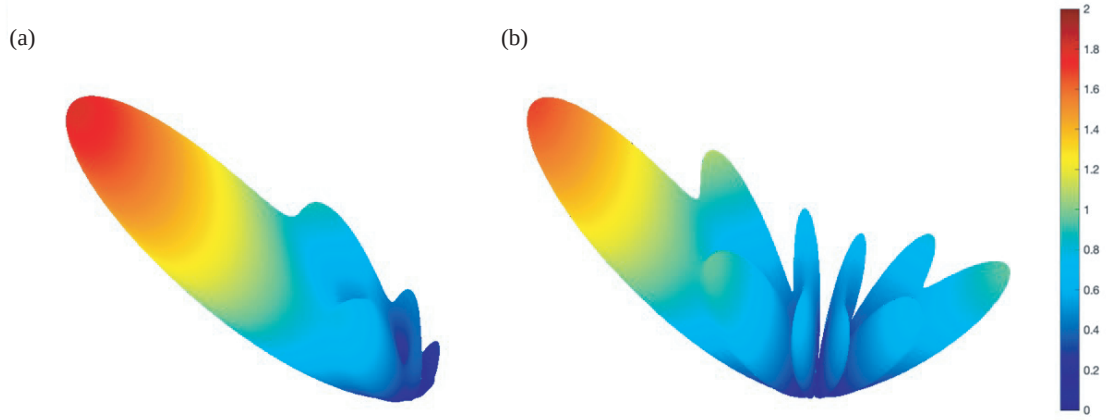


**FIGURE 3**. 3-D far-field radiation patterns of c-OAM beams generated by (a) CASM ($a = 0.06\,\text{m}$, $l_o = 8$, $N = 360$, $M = 101$) and (b) DASM ($a = 0.06\,\text{m}$, $l_o = 8$, $N = 18$, $M = 6$) at 10 GHz.

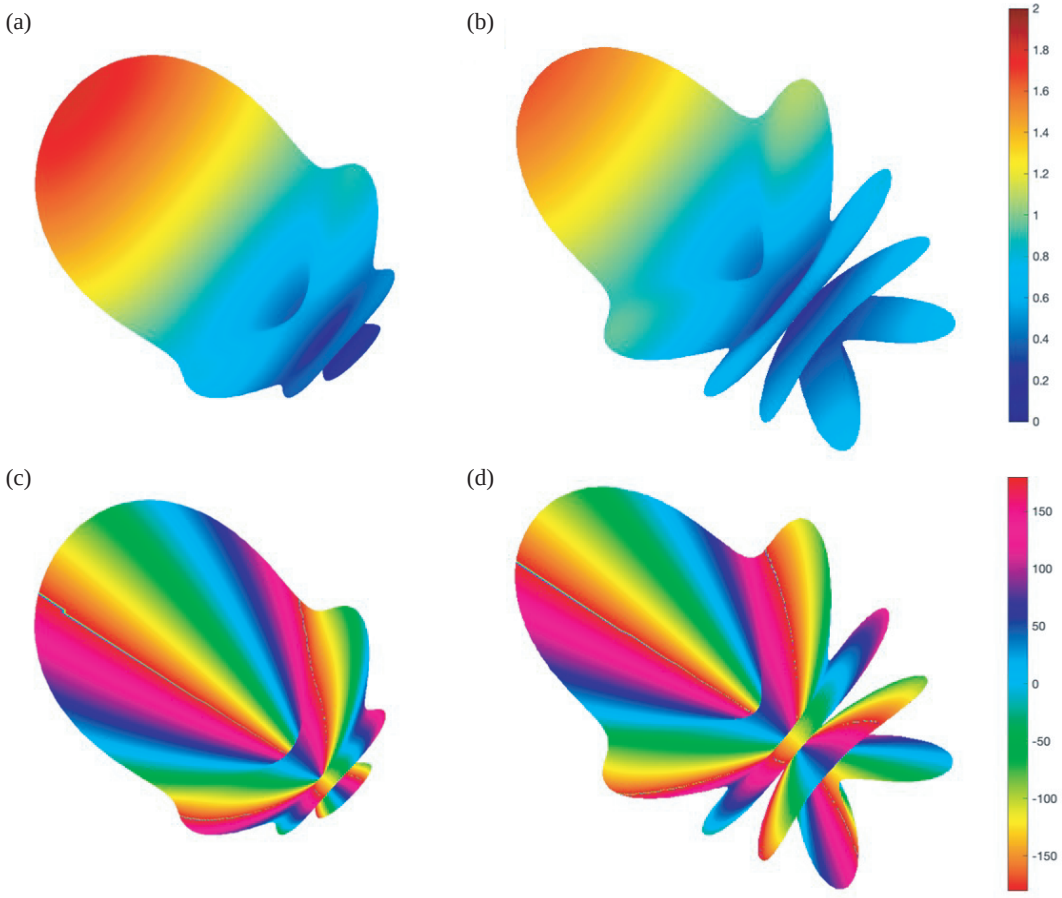


**FIGURE 4**. 2-D intensity (upper) and phase (bottom) distributions of c-OAM beams generated by (a) (c) CASM ($a = 0.06\,\text{m}$, $l_o = 8$, $N = 360$, $M = 101$) and (b) (d) DASM ($a = 0.06\,\text{m}$, $l_o = 8$, $N = 18$, $M = 6$) at 10 GHz.

To further show that c-OAM is a directional beam with vorticity in the main lobe, Fig. 5(a) and Fig. 5(b) demonstrate the amplitude distributions, phase distributions, and normalized angular radiation patterns of CASM and DASM, respectively. In sub-pictures of Fig. 5, amplitude distribution is shown on the left top with a purple solid line; phase distribution is shown on the left bottom with a green dotted line; and the normalized angular radiation pattern is shown on the right top with an orange solid line. Additionally, the angular radiation patterns shown on the right bottom with blue solid lines in Figs. 5(a) and (b) are obtained by the derived field expressions (3) and (7), respectively. The simulation results are consistent with the

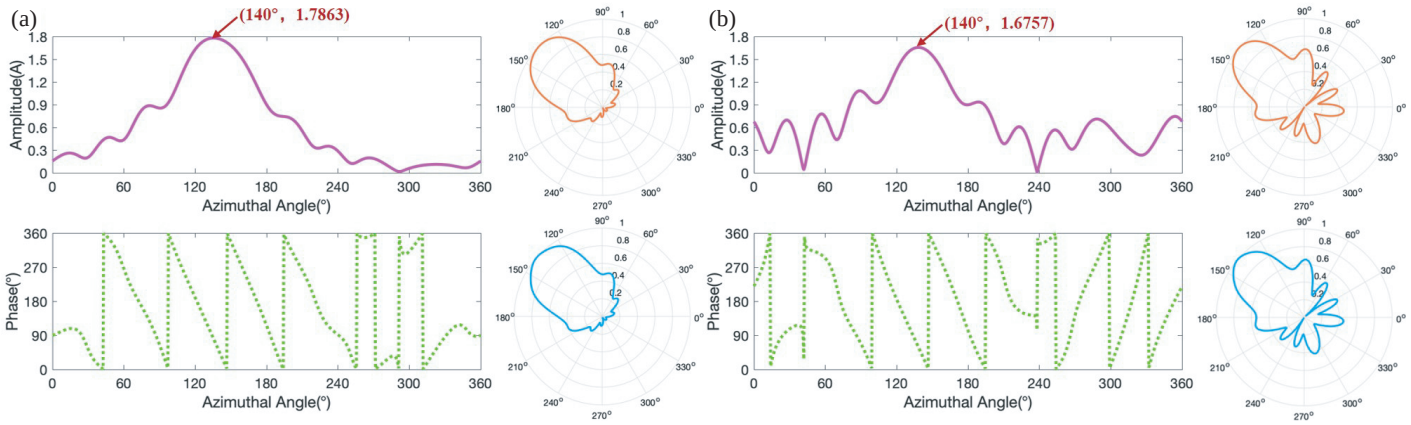


**FIGURE 5**. Amplitude distributions, phase distributions and normalized angular radiation patterns of c-OAM beams generated by (a) CASM ($a = 0.06\,\text{m}$, $l_o = 8$, $N = 360$, $M = 101$) corresponding to (3) and (b) DASM ($a = 0.06\,\text{m}$, $l_o = 8$, $N = 18$, $M = 6$) corresponding to (7).

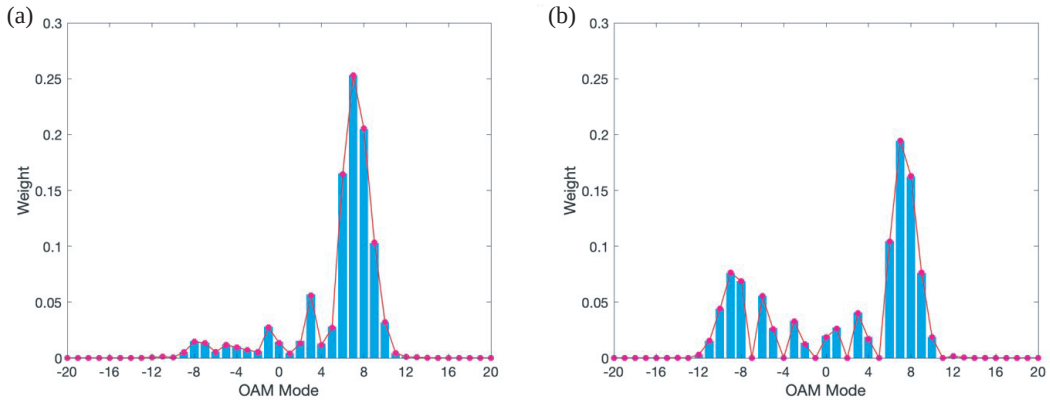


**FIGURE 6**. OAM spectra of c-OAM beams generated by (a) CASM ($a = 0.06\,\text{m}$, $l_o = 8$, $N = 360$, $M = 101$) corresponding to (3) and (b) DASM ($a = 0.06\,\text{m}$, $l_o = 8$, $N = 18$, $M = 6$) corresponding to (7).

deduced results, proving the correctness of the derived electric field expressions. The little difference is boiled down to that the higher-order terms are omitted from the formula. From Fig. 5(a) and Fig. 5(b), we can plainly figure out that both beams have gain, and the phase distributions are linear in the main lobes of the beams. Because the energy is concentrated in the main lobe, and the phase is linear in the main lobe, the c-OAM beams have vorticity and quasi-orthogonality. The calculation of orthogonality is actually the calculation of correlation [15]. Thus, quasi-orthogonality of c-OAM beams is also the calculation of correlation. Comparing Fig. 5(a) with Fig. 5(b), we can find that the c-OAM beam generated by DASM has a side lobe, and the phase slope in the side lobe is opposite to that of the main lobe. This can be well explained by the following OAM spectral analysis results.

Figure 6 shows the OAM spectra of the c-OAM beams. The blue columns represent the OAM mode distributions analyzed by the electric fields obtained by numerical simulations, while the red dots represent the OAM mode distributions derived by (3) and (7), respectively. The simulation results and derivation results are consistent, which proves the rationality of theoretical analysis. In Fig. 6, there are many adjacent side modes except the main mode. This explains why CASM and DASM could generate directional beams. The directional beams can be considered as the superposition of these OAM beams with different modes. For the case of DASM, OAM modes extend periodically with a period of $N$ according to (6). In the simulation, $N = 18$, $l_o = 8$, thus, relatively high adjacent side modes will appear near mode $-10$, just as shown in Fig. 6(b). This intuitively explains why c-OAM beams generated by DASM have side lobes, and the phase distribution of the side lobe changes in the opposite direction to that of the main lobe. It is worth noting that the value of the phase slope is determined by the superposed OAM modes and their weights, and the mode with the highest weight in the OAM spectra depends on the magnitude factor of the electric field $\text{sinc}[\beta(l - l_o)/2] \cdot J_l(ka\sin\theta)$. When $l = l_o$, the value of the item sinc achieves maximum 1. However, the item *Bessel* is not only associated with the order $l$, but also associated to the arc radius $a$ and elevation angle $\theta$. Besides, *Bessel* function itself is oscillating. Thus, the desired mode $l_o$ is not necessarily the mode with the highest weight. That is why modes with the highest weight in Figs. 6(a) and (b) are not 8. As the number of the array elements increases, the period becomes larger, and mode interval becomes larger, then multiplied by the corresponding weighting factor, the side lobe becomes smaller gradually. In Fig. 7, angular radiation patterns

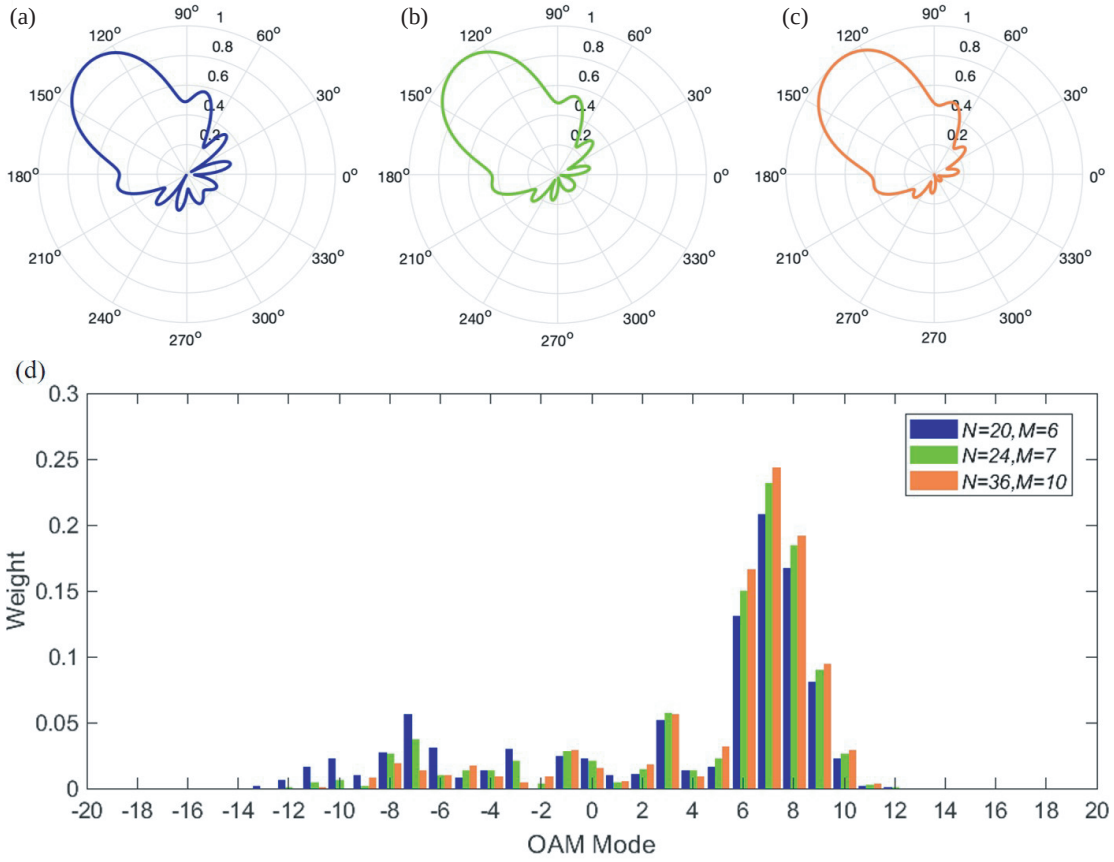


**FIGURE 7**. Angular radiation patterns of c-OAM beams generated by DASM ($a = 0.06\,\text{m}$, $l_o = 8$) with the same central angle ($\beta = 90°$) but different numbers of array elements; (a) $N = 20$, $M = 6$; (b) $N = 24$, $M = 7$; (c) $N = 36$, $M = 10$; (d) OAM spectra of the c-OAM beams corresponding to (a) (b) (c).

of c-OAM beams generated by DASM ($a = 0.06\,\text{m}$, $l_o = 8$, $\beta = 90°$) with different numbers of array elements are shown in Figs. 7(a) (b), (c), Fig. 7(a) is the case of $N = 20$, $M = 6$ (blue), Fig. 7(b) the case of $N = 24$, $M = 7$ (green), Fig. 7(c) the case of $N = 36$, $M = 10$ (orange), and Fig. 7(d) shows the OAM spectra of the c-OAM beams corresponding to Figs. (a), (b), (c). The central angles of the three cases are all 90°. The side lobe of the generated c-OAM beam becomes smaller as the number of the array elements increases, as shown in Figs. 7(a), (b), (c). It can be well explained by the OAM spectra in Fig. 7(d). In the main mode area, the weight of the mode in orange is higher than that in green, and the weight of the mode in green is higher than that in blue, but in the side mode area, it is the other way around. In a word, the higher the mode weight is in the main mode area and the lower the mode weight is in the side mode area, the smaller the side lobe of the beam is. In all, better parameter selection will lead to better results, and the greater the weight of the OAM mode is, the greater the impact is on the generated c-OAM beam, especially in terms of phase.

It is obviously shown in Fig. 4 and Fig. 5 that c-OAM beams have vorticity. However, orthogonality is also an extremely vital property of traditional OAM waves. According to OAM spectra analysis, the c-OAM beam can be regarded as the superposition of OAM waves with different modes; when there is no overlap between the decomposed OAM modes of two c-OAM beams, it is easy to verify that the two beams are orthogonal [15]. Since the c-OAM beam's energy is mainly concentrated in the main lobe, and the phase is linear in the main lobe, it is exciting to find that c-OAM beams have quasi-orthogonality. Taking two c-OAM beams as an example: one is the c-OAM beam shown in Fig. 5(a), and the other is the c-OAM beam simulated with $l_o = -8$ and rotated by 180°. The correlation coefficient between them is 0.0549. The quasi-orthogonality and vorticity of c-OAM beam make it more suitable for OAM property based practical applications.

It is worth discussing the beam directions of the c-OAM beams generated by CASM and DASM. Observing the electric field expressions derived in Section 2, we can find that all electric field components have the term $j^l e^{-jl\varphi} J_l(ka\sin\theta)$, and deriving the term further, it can be written as $\exp(-jl(\varphi - \frac{\pi}{2} \cdot l/|l|)) \cdot J_{|l|}(ka\sin\theta)$. According to the term, we can deduce the azimuth direction of the c-OAM beams. When mode $l$ is positive, the azimuth direction of the beam is 90° counterclockwise relative to the center position of the arc. When mode $l$ is negative, the azimuth direction of the beam is 90° clockwise relative to the center position of the arc. Just as shown in Fig. 8, the red beam A represents the c-OAM beam generated by CASM and DASM. $\widehat{ABC}$ is an arc wire with electric current $I_0 e^{-jl_o\varphi}$; the arc's central angle is $\beta$; $A$ is the start point; $B$ is the end point;

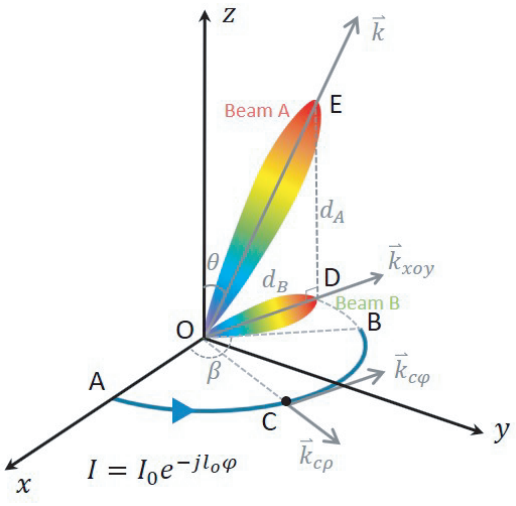


**FIGURE 8**. The schematic of c-OAM beams' direction and transmission distance.

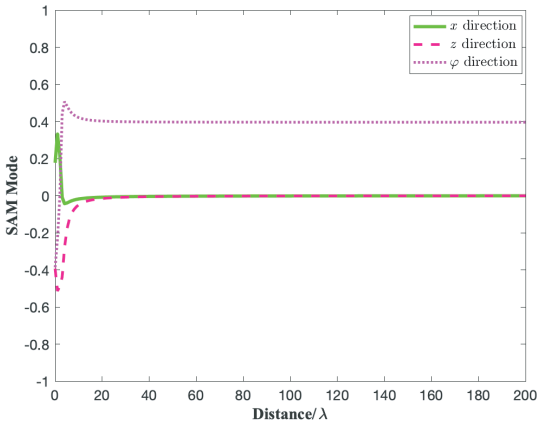


**FIGURE 9**. Simulated SAM modes versus transmitting distance.

$C$ is the midpoint; $\vec{k}_{c\rho}$ and $\vec{k}_{c\varphi}$ are radial vector and tangential vector of point $C$ on the arc, respectively. When $l_o$ is positive, the azimuth direction of the c-OAM beam is $\overrightarrow{OD}$, i.e., the projection $\vec{k}_{xoy}$ of the beam direction $\vec{k}$ in $xoy$ plane. When $l_o$ is negative, the azimuth direction of the c-OAM beam is $\overrightarrow{DO}$. Since the central angles of the CASM and DASM simulated in Figs. 2(a) and (b) are 100°, the azimuth angles of the generated c-OAM beams are 140°, which are the directions of $k_{\varphi s}$ and $k_{\varphi d}$, shown in Fig. 2, and can be verified in Figs. 5(a) and (b). In a word, the azimuth direction is only related to positive or negative that the OAM mode is, and has nothing to do with the value of the mode. The elevation angle $\theta_m$ of the c-OAM beam satisfies the formula $\sin\theta_m = \xi_l/(ka)$, where $\xi_l$ is the first pole of the $l$-th *Bessel* function, $k$ the wave number, and $a$ the arc radius. The larger the radius is, the smaller the elevation angle is, and vice versa. Hence, beam direction is determined if the antenna radius and its placement are both determined. The experimental results in [18] have also verified the conclusion of the beam direction analyzed above.

Polarization is a significant property of electromagnetic beams. CASM is equivalent to $\varphi$-orientation DASM when the number of the array elements is enough. Thus, we studied the polarization of c-OAM beams generated by $z$-orientation, $x$-orientation, and $\varphi$-orientation DASM. The simulation parameters are set as follows, $l_o = 8$, $a = 0.06\,\mathrm{m}$, $N = 48$, $M = 16$. The spin angular momentum (SAM) of the electromagnetic field can be calculated by Stokes formula [24]

$$\mathbf{s} = \frac{\mathrm{Im}\left(\frac{\varepsilon}{2}\mathbf{E}\times\mathbf{E}^* + \frac{\mu}{2}\mathbf{H}\times\mathbf{H}^*\right)}{w} \tag{12}$$

where $w = (\varepsilon|\mathbf{E}|^2 + \mu|\mathbf{H}|^2)/2$, representing the energy density of the radiated field. Fig. 9 shows the simulated SAM modes versus transmitting distance. The radiation field changes from right-handed elliptical polarization to left-handed elliptical polarization and then to linear polarization for the case of $x$-orientation, just as the green solid line shown in Fig. 9. The radiation field changes from left-handed elliptical polarization to linear polarization for the case of $z$-orientation, just as the red dotted line shown in Fig. 9. The radiation field changes from left-handed elliptical polarization to right-handed elliptical polarization for the case of $\varphi$-orientation, just as the purple dotted line shown in Fig. 9. In more detail, the radiation field maintains a stable polarization state when the propagation distance exceeds $10\lambda$, where $x$-, $z$-orientation corresponds to linear polarization, and $\varphi$-orientation corresponds to right-handed elliptical polarization. Consequently, c-OAM beams are compatible with current polarization multiplexing technology when it comes to practical application. The $x$-, $z$-orientation DASMs are more suitable for polarization multiplexing than $\varphi$-orientation DASM and CASM in long-distance propagation communication systems.

In this section, the properties of the c-OAM beams generated by CASM and DASM are analyzed in detail. The c-OAM beams have directional gain, and the phase distributions are linear in the main lobes. From the OAM spectra analysis, c-OAM beams can be regarded as radio beams superposed by several OAM beams with certain amplitudes and phases, and the beam properties could be boiled down to OAM spectra distributions. Most importantly, the correctness of the field distribution formula derived mathematically in Section 2 is verified through the analysis of the numerical simulation results.

## 4. COMPARISON AND POTENTIAL APPLICATIONS

The indirect method of generating c-OAM beams is to superpose several independent PS-OAM waves together [14]. Quantities of PS-OAM antennas are required, and it is hard to generate c-OAM beams with equivalent high order OAM mode. While CASM and DASM proposed in this paper can generate c-OAM beams directly, the antenna could be compact and simple [18, 19]; the generated c-OAM beams are directional beams; the black holes in the center of OAM waves are avoided due to the directional gains. c-OAM beams superposed by PS-OAM

waves are in the horizontal plane [14, 15], and the elevations of the beams are 90°, just as the green beam B show in Fig. 8. While c-OAM beams generated by CASM and DASM are usually spatial beams radiating to 3-D space, just as the red Beam A shown in Fig. 8, its elevation angle is $\theta$ ($0° < \theta \leq 90°$). However, when the arc radius is small enough, beam A will radiate in the horizontal plane too. Suppose that the transmitting distance of beam A is $d_A$, as the dotted line shown in Fig. 8, and the transmitting distance of beam B is $d_B$, as the solid line shown in Fig. 8; since $d_A = d_B / \tan\theta$, the transmitting distance of beam A is larger than that of beam B when the antenna receiving aperture is the same.

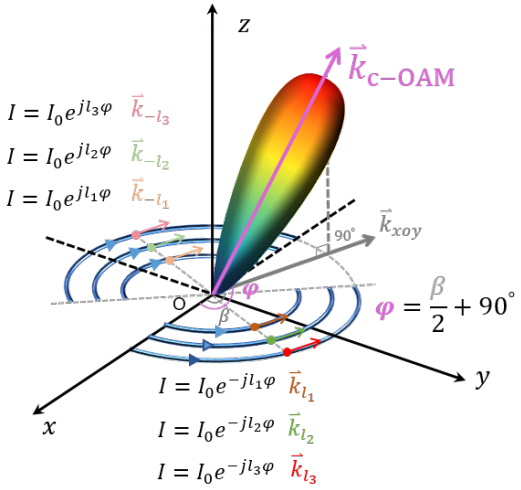


**FIGURE 10**. The schematic of the principled MIMO architecture.

Since the c-OAM beams have vorticity and quasi-orthogonality, the communication technologies based on OAM are also suitable. A principle MIMO architecture based on CASM or DASM is presented in Fig. 10. Multiple CASM antennas are centro-symmetrically placed on the same plane, and symmetric antennas have opposite modes. By adjusting the arc radius of these antennas, the generated beams will have the same directivity, as the direction of $\vec{k}_{u-OAM}$ shown in Fig. 10, thus could be used for mode multiplex. Taking advantages of beamforming realized directly at the transmitting end through antenna architecture, the signal to noise ratio (SNR) of communication systems will be improved.

## 5. CONCLUSION

In this paper, CASM and DASM are proposed to form a systematic theory to generate c-OAM beams directly. Compared with OAM beams whose radiation patterns are like 'donut', c-OAM beams are directional beams with high gain. They retain vorticity of OAM in the main lobes and have quasi-orthogonality.

The methods of generating c-OAM beams are summarized, and mathematical models of CASM and DASM are demonstrated. Current distribution expressions of CASM and $x$, $z$, $\varphi$ orientation DASMs are described, by conducting Fourier series expansion on them, the field expressions of the generated c-OAM beams are derived clearly. By numerical simulations, far-field, $E$-field, amplitude and phase distributions of the c-OAM beams are obtained. OAM spectra distributions are also analyzed and certify the correctness of the derived field expressions. In addition, beam direction and polarization of the c-OAM beams are discussed.

A principle MIMO architecture based on CASM and DASM is proposed. It is evident that c-OAM beams could avoid the inherent puzzles of OAM beams, meanwhile have vorticity and quasi-orthogonality. Taking advantage of the directional gain, it can reduce the waste of signal energy and improve the SNR when c-OAM beams are applied in communication systems, and it becomes easier to receive the most energy of the beam within a limited receiving antenna aperture. In a word, CASM and DASM theory which is capable of generating c-OAM beams will provide a more practical scheme for OAM property based applications.

## ACKNOWLEDGEMENT

This work was supported by the National Natural Science Foundation of China under Grant 62171409, Grant 61571391 and Grant 61371030.

## REFERENCES

[1] Gesbert, D., M. Shafi, D.-S. Shiu, P. J. Smith, and A. Naguib, "From theory to practice: An overview of MIMO space-time coded wireless systems," *IEEE Journal on Selected Areas in Communications*, Vol. 21, No. 3, 281–302, Apr. 2003.

[2] Vook, F. W., A. Ghosh, and T. A. Thomas, "MIMO and beamforming solutions for 5G technology," in *2014 IEEE MTT-S International Microwave Symposium (IMS2014)*, 1–4, Tampa, FL, USA, Jun. 2014.

[3] Allen, L., M. W. Beijersbergen, R. J. C. Spreeuw, and J. P. Woerdman, "Orbital angular momentum of light and the transformation of Laguerre-Gaussian laser modes," *Physical Review A*, Vol. 45, No. 11, 8185, Jun. 1992.

[4] Fürhapter, S., A. Jesacher, S. Bernet, and M. Ritsch-Marte, "Spiral phase contrast imaging in microscopy," *Optics Express*, Vol. 13, No. 3, 689–694, Feb. 2005.

[5] Huang, H., G. Xie, Y. Yan, N. Ahmed, Y. Ren, Y. Yue, D. Rogawski, M. J. Willner, B. I. Erkmen, K. M. Birnbaum, S. J. Dolinar, M. P. J. Lavery, M. J. Padgett, M. Tur, and A. E. Willner, "100 Tbit/s free-space data link enabled by three-dimensional multiplexing of orbital angular momentum, polarization, and wavelength," *Optics Letters*, Vol. 39, No. 3, 197–200, Jan. 2014.

[6] Yan, Y., G. Xie, M. P. J. Lavery, H. Huang, N. Ahmed, C. Bao, Y. Ren, Y. Cao, L. Li, Z. Zhao, A. F. Molisch, M. Tur, M. J. Padgett, and A. E. Willner, "High-capacity millimetre-wave communications with orbital angular momentum multiplexing," *Nature Communications*, Vol. 5, No. 1, 4876, Sep. 2014.

[7] Zhang, W., S. Zheng, X. Hui, R. Dong, X. Jin, H. Chi, and X. Zhang, "Mode division multiplexing communication using microwave orbital angular momentum: An experimental study," *IEEE Transactions on Wireless Communications*, Vol. 16, No. 2, 1308–1318, Feb. 2017.

[8] Thidé, B., H. Then, J. Sjoholm, K. Palmer, J. Bergman, T. D. Carozzi, Y. N. Istomin, N. H. Ibragimov, and R. Khamitova, "Utilization of photon orbital angular momentum in the low-frequency radio domain," *Physical Review Letters*, Vol. 99, No. 8, 087701, Aug. 2007.

[9] Tamburini, F., E. Mari, A. Sponselli, B. Thidé, A. Bianchini, and F. Romanato, "Encoding many channels on the same frequency through radio vorticity: First experimental test," *New Journal of Physics*, Vol. 14, No. 3, 033001, Mar. 2012.

[10] Zhang, W., S. Zheng, Y. Chen, X. Jin, H. Chi, and X. Zhang, "Orbital angular momentum-based communications with partial arc sampling receiving," *IEEE Communications Letters*, Vol. 20, No. 7, 1381–1384, Jul. 2016.

[11] Zhang, Z., S. Zheng, J. Zheng, X. Jin, H. Chi, and X. Zhang, "Plane spiral orbital angular momentum wave and its applications," in *2016 IEEE MTT-S International Microwave Symposium (IMS)*, 1–4, San Francisco, CA, USA, May 2016.

[12] Yao, E., S. Franke-Arnold, J. Courtial, S. Barnett, and M. Padgett, "Fourier relationship between angular position and optical orbital angular momentum," *Optics Express*, Vol. 14, No. 20, 9071–9076, Oct. 2006.

[13] Jack, B., M. J. Padgett, and S. Franke-Arnold, "Angular diffraction," *New Journal of Physics*, Vol. 10, 103 013–103 021, Oct. 2008.

[14] Wang, Z., S. Zheng, X. Xiong, Z. Zhu, Y. Chen, X. Yu, X. Jin, and X. Zhang, "Structure radio beam construction in azimuthal domain," *IEEE Access*, Vol. 8, 9395–9402, 2020.

[15] Zheng, S., Y. Chen, Z. Zhang, X. Jin, H. Chi, X. Zhang, and Z. N. Chen, "Realization of beam steering based on plane spiral orbital angular momentum wave," *IEEE Transactions on Antennas and Propagation*, Vol. 66, No. 3, 1352–1358, Mar. 2018.

[16] Wang, X., S. Zheng, X. Yu, X. Jin, and X. Zhang, "A compact PSOAM antenna based on substrate integrated waveguide," *Journal of Communications and Information Networks*, Vol. 4, No. 3, 18–24, 2019.

[17] Zhu, Z., S. Zheng, X. Xiong, Y. Chen, X. Jin, X. Yu, and X. Zhang, "A compact pattern reconfiguration antenna based on multimode plane spiral OAM," *New Journal of Physics*, Vol. 6, No. 9, 1168–1172, 2021.

[18] Fouda, R. M., T. C. Baum, and K. Ghorbani, "Quasi-orbital angular momentum (Q-OAM) generated by quasi-circular array antenna (QCA)," *Scientific Reports*, Vol. 8, No. 1, 8363, May 2018.

[19] Xiong, X., S. Zheng, Z. Zhu, Z. Wang, Y. Chen, X. Yu, and X. Zhang, "Direct generation of OAM mode-group and its application in LoS-MIMO system," *IEEE Communications Letters*, Vol. 24, No. 11, 2628–2631, Nov. 2020.

[20] Zheng, S., X. Hui, X. Jin, H. Chi, and X. Zhang, "Transmission characteristics of a twisted radio wave based on circular traveling-wave antenna," *IEEE Transactions on Antennas and Propagation*, Vol. 63, No. 4, 1530–1536, Apr. 2015.

[21] Liu, K., Y. Cheng, Y. Gao, X. Li, Y. Qin, and H. Wang, "Superresolution radar imaging based on experimental OAM beams," *Applied Physics Letters*, Vol. 110, No. 16, 164102, Apr. 2017.

[22] Lavery, M. P. J., F. C. Speirits, S. M. Barnett, and M. J. Padgett, "Detection of a spinning object using light's orbital angular momentum," *Science*, Vol. 341, No. 6145, 537–540, Aug. 2013.

[23] Zhu, Z., S. Zheng, X. Xiong, Y. Chen, X. Hui, X. Jin, X. Yu, and X. Zhang, "A non-uniform travelling-wave current source model for designing OAM antenna: Theory, analysis and application," *IEEE Access*, Vol. 10, 47 499–47 508, 2022.

[24] Carozzi, T., R. Karlsson, and J. Bergman, "Parameters characterizing electromagnetic wave polarization," *Physical Review E*, Vol. 61, No. 2, 2024, 2000.